Processing and characterization of elastic and thermal expansion behaviour of interpenetrating Al12Si/alumina composites

Siddhartha Roy, Karl Günter Schell, Ethel Claudia Bucharsky, Kay A. Weidenmann, Alexander Wanner, Michael J. Hoffmann

Roy, Siddhartha, Karl Günter Schell, Ethel Claudia Bucharsky, Kay A. Weidenmann, Alexander Wanner, and Michael J. Hoffmann. 2019. "Processing and characterization of elastic and thermal expansion behaviour of interpenetrating Al12Si/alumina composites." *Materials Science and Engineering: A* 743: 339–48. https://doi.org/10.1016/j.msea.2018.11.100.

Processing and characterization of elastic and thermal expansion behaviour of interpenetrating Al12Si/alumina composites

Siddhartha Roy[a,b,*], Karl Günter Schell[c], Ethel Claudia Bucharsky[c], Kay André Weidenmann[a], Alexander Wanner[a], Michael J. Hoffmann[c]

[a] *Institute for Applied Materials (IAM-WK), Karlsruhe Institute of Technology, Karlsruhe 76131, Germany*
[b] *Department of Metallurgical and Materials Engineering, Indian Institute of Technology Kharagpur, 721302 India*
[c] *Institute for Applied Materials – Ceramic Materials and Technologies (IAM-KWT), Karlsruhe Institute of Technology, 76131 Germany*

1. Introduction

Metal matrix composites (MMC) typically combine a dispersed ceramic reinforcement in a metallic alloy matrix. They are technologically attractive because of their enhanced specific properties with respect to the unreinforced metallic alloy and enhanced ductility and toughness in comparison to the ceramic reinforcement [1–3]. In terms of the shape of the reinforcement, MMCs can be classified into several groups – particle reinforced, short fiber reinforced, continuous fiber reinforced, interpenetrating composites etc. [4]. Among them, particle reinforced, short fiber reinforced and continuous fiber reinforced composites have been studied quite extensively over the last several decades and their processing – microstructure – mechanical property correlations are relatively well understood [5–14]. Highest property enhancement is obtained in continuous fiber reinforced composites. These composites are however very anisotropic and transverse to fiber direction, the properties are rather poor. Particle reinforced composites have the advantage that they are almost isotropic, however; their property enhancement with respect to the unreinforced metallic matrix is limited. Property enhancement in short fiber reinforced composites is also limited and they are mostly isotropic only in the plane of the fibers.

Interpenetrating phase composites (IPC), in which both metallic and ceramic phases are co-continuous in three dimensions, offer better strength, stiffness and wear resistance with respect to particle reinforced composites at both room and elevated temperatures [15–17]. Additionally, as in IPCs there is no preferred orientation of the matrix and reinforcing phases, the composites are predominantly isotropic. Moreover, Roudini et al. [18] have shown that both the thermal expansion coefficient and the extent of thermal hysteresis in composites decrease as the contiguity of the reinforcement phase increases. These favourable properties along with the fact that in IPCs it is readily possible to alter their properties by tailoring the amounts and morphologies of individual phases, have resulted in significant research emphasis in recent times. These include IPCs fabricated by reaction synthesis [19–21], by melt infiltration in wood ceramics [22], in 3-D periodic preforms produced by robotic deposition [23], in porous ceramic preforms fabricated by freeze-casting [24–26], in porous ceramic preforms fabricated using cellulose fibers as pore formers [27–29], in porous ceramic preforms using polyurethane foams as starting material [30] etc.

---

[*] Corresponding author at. Department of Metallurgical and Materials Engineering, Indian Institute of Technology Kharagpur, 721302 India
E-mail address: siddhartha@metal.iitkgp.ac.in (S. Roy).

In spite of these recent advances, there is still scope for further improvement in terms of developing cost efficient processing routes and tailoring phase morphologies to optimise final material properties of IPCs. The current authors recently proposed a simple route to fabricate open porous silicon carbide (SiC) ceramic bodies with a wide range of porosity and pore morphology using two different polymer waxes in various mixture ratios as pore formers [31,32]. This technique allows varying both the ceramic content as well as the pore morphology over wide ranges. In these earlier studies thorough characterization of the elastic properties of the fabricated preforms were carried out. However, to the best of the knowledge of the authors, no study has been carried out until now on metal/ceramic composites based on these porous preforms. In this work the same processing technique was utilized to first fabricate open porous alumina preforms. These preforms were subsequently infiltrated with near eutectic Al12Si melt to fabricate the metal/ceramic IPCs. Thorough structural characterization of both preforms and IPCs was carried out using optical microscope (only for the IPC), scanning electron microscope and X-ray computed tomography (only for the ceramic preforms). Detailed characterization of the elastic properties of both porous preforms and IPC was done using non-destructive ultrasound phase spectroscopy. Low thermal expansion coefficient (CTE) of IPCs being one of its prime advantageous properties, CTE of the IPCs was determined for different ceramic contents between room temperature and 500 °C. Results obtained from composite elastic property analysis as well as CTE measurement have been compared with the predictions from numerous theoretical model predictions. This way, a thorough in depth study of this new interpenetrating phase composite material is performed.

2. Experimental procedure

2.1. Processing of porous alumina preforms

Alumina powder “CL 2500” with average particle size of 1.7 µm from Almatis Premium Alumina, LA, USA was used as ceramic powder. Two different polymer waxes – large “Viscowax 112” with $d_{50} = 150$ µm and density 0.93–0.95 g/cc from Innospec Inc., Germany (hereafter referred to as VW) and fine “Ceridust 3620” with $d_{50} = 7.5–9.5$ µm and density 0.96–0.98 g/cc from Clariant AG, Switzerland (hereafter referred to as CD) were used as pore formers. To enhance the stability of the green preforms, the alumina powders were initially pre-treated in a suspension. The powder was first mixed with the dispersant Dolapix CE 64 (0.19 wt%) and then a suspension was prepared in 1% polyvinyl alcohol (PVA) by mixing using a magnet rotor for two hours. PVA acts as a binder which decomposes at higher dissociation temperatures than the pore formers. After subsequent freeze-drying to remove the moisture, the powder was ready for further processing steps.

Three different mixture ratios of total polymer wax: pre-treated alumina powder were used (50:50, 60:40 and 70:30 vol%, respectively) while in each mixture the two different pore formers VW and CD were mixed in 1:1 ratio (refer to [32]). The powder mixtures were first ball-milled for 10 min using zirconium oxide balls. Subsequently they were uni-axially pressed under 40 MPa (precision hydraulic press with capacity 100 t, manufactured by Paul-Otto Weber GmbH, Germany) to produce green bodies.

The green bodies were subsequently burnt and sintered to have sufficient strength for infiltration. Burning and sintering were done in multiple steps. They were first heated up to 150 °C at a very slow rate of 0.2 °C/min. The polymer waxes melt at this temperature. After holding for 30 min, the temperature was raised to 250 °C at a rate of 0.75 °C/min. PVA starts volatilizing during this step. To make sure that no residue from either the pore formers or the binder remain in the green body, the green bodies were further heated up to 600 °C at a rate of 3 °C/min. After a holding period of 15 min, heating of the oven was switched off. Throughout the burning process step, the oven was purged with air. The burnt preforms were subsequently placed inside the sintering oven very carefully to make sure no damage of the fragile preforms occurred during handling. Sintering was carried out under normal atmosphere. For sintering, the temperature was first raised to 200 °C at a rate of 3 °C/min and subsequently it was raised to 1550 °C at a rate of 5 °C/min. After holding at this sintering temperature for two hours, the temperature was reduced to room temperature at a rate of 10 °C/min.

2.2. Fabrication of interpenetrating metal/ceramic composites

To fabricate the IPCs, the porous preforms were infiltrated by liquid Al12Si using inert gas pressure infiltration. The porous preforms along with billets of the metallic alloy were placed inside a pressure chamber. To facilitate infiltration, the chamber was first evacuated to remove all the air from the pores within the preforms. The temperature inside the chamber was then raised to 750 °C to bring Al12Si into molten state. In the molten state the liquid metal completely covers the porous ceramic preform. After a vacuum hold period of 20–30 min, high pressure in the range of 40–100 bar was applied by inert argon gas to carry out the melt infiltration. After infiltration was complete, the pressure was maintained as the temperature was reduced to room temperature to allow the metallic alloy to solidify. Finally, the pressure was released and the infiltrated composite was cut from the surrounding cast metal by diamond wheel cutting.

2.3. Structural characterization

The amounts of open, closed and total porosity in the ceramic preforms were calculated by measuring the density of the samples following Archimedes principle, by immersing in water. This technique was also used to determine the densities of the fabricated composite samples. SEM analysis of the preforms and the composites was carried out using a SEM Zeiss EVO 50 (Oberkochen, Germany) and micro CT analysis of the preforms was carried out using a CT system of type Y.CT PRECISION from YXLON International GmbH, Hamburg, Germany. For micro CT analysis, the voxel side length was in the range of 4–5 µm.

2.4. Determination of elastic constants

Ultrasound phase spectroscopy (UPS) was used to determine the elastic constants of the porous preforms and the IPC. Only longitudinal elastic constants are reported for the porous preforms, while both longitudinal and shear elastic constants are reported for the IPC.

Although UPS is a rather robust technique for determination of longitudinal and shear elastic constants in a wide range of porous and multiphase materials (as depicted in [25,28,31,33,34]), this method is not used very widely. Hence, a brief overview of the theory and the method is provided here and for thorough description we refer to [35–38].

An undamped plane monochromatic wave propagating along x-axis can be written as:

$$u(x,t) = u_0 \bullet e^{i(\omega t + kx)} \tag{1}$$

where $(\omega t + kx)$ is the phase function, $\omega = 2\pi f$ is the circular frequency and $k = 2\pi/\lambda$ is the wave number. A pulse being a superposition of many waves, in a sample of length L, the group velocity can be defined as

$$V_g = \frac{d\omega}{dk} = L \bullet \frac{df}{dN} \tag{2}$$

where N is the number of wave periods in the sample. The phase difference between the received and the input signals $\Delta\phi$ is related to N according to

$$\Delta\phi = -2\pi \mathrm{N} \tag{3}$$

Combining Eqs. (2) and (3), the expression for the group velocity (V_g) is written as

$$V_g = -\frac{2\pi L}{(d\Delta\varnothing/df)} \tag{4}$$

If the phase change of the propagating wave in a sample is measured continuously by increasing its frequency, then the denominator on the right hand side of Eq. (4) denotes the slope of the phase-frequency spectrum. For a non-dispersive material, the sound velocity is independent of frequency and for such samples the phase-frequency spectrum becomes a straight line with a constant slope over the complete range of measurement.

Once the group velocity (V_g) is measured as described above, the corresponding elastic constant (C_{ii}) along the material direction of wave propagation can be calculated according to the equation

$$C_{ii} = \rho V_g^2 \tag{5}$$

where ρ is the sample density.

The elastic constants C_{ii} are the elements of the stiffness matrix and they are different from the more well-known Young's modulus of a material. Along any material direction C_{ii} is a function of the corresponding Young's modulus and the Poisson's ratio [39]. C_{ii} is generally higher than the Young's modulus and for an isotropic material with a Poisson's ratio of approximately 0.25, this difference is about 20%.

The schematic of the basic experimental setup employed in this work to determine the group velocities of the propagating waves is shown in Fig. 1. Two broadband ultrasonic transducers (longitudinal or shear) of the same kind are attached to the two opposite faces of a plane parallel sample using an ultrasonic couplant. One of the transducers acts as transmitter and the other one as receiver of ultrasonic signal. Continuous, harmonic and elastic waves are generated by a network analyser and the phase as well as the amplitude shift between the incident and the transmitted waves is continuously measured. All electronic components necessary for measurement of phase and amplitude shown in Fig. 1, are included in the network analyser.

The measurements in this work were accomplished using an electronic network analyser (Advantest, model R3754A) and two identical broadband piezoelectric transducers (Panametrics, model V122 with nominal central frequency 7.5 MHz and diameter 9.5 mm for longitudinal elastic constants and model V155 with nominal central frequency 5 MHz and diameter 12.7 mm for shear elastic constants). The samples studied in this work had rectangular parallelepiped shapes with side lengths in the range of 5–9 mm. For longitudinal elastic constants, the phase and amplitude spectra were recorded in the frequency range from 10 kHz to 15 MHz; while for shear elastic constants the same range was from 10 kHz to 10 MHz. The apparent phase and amplitude shifts measured during any measurement is the sum of the shift actually caused by the sample being studied as well as the frequency dependent shifts caused by the transducers and the electronic system of the setup used. To properly calibrate the setup to only determine the shifts caused by the sample, measurements were first performed with only the two transducers in contact with each other through the couplant but without any sample between them. The corresponding shifts were subtracted from the actual measurements with the sample to determine only the shifts due to the sample being measured.

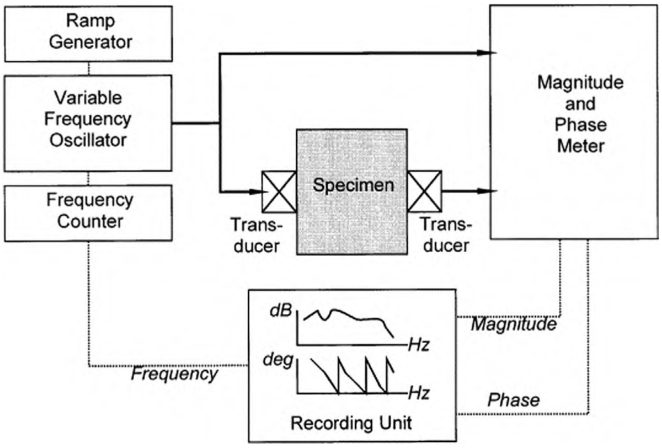

Fig. 1. Schematic of the ultrasonic test setup used in this work for UPS measurements (reproduced from [35] with permission from Elsevier).

The following co-ordinate system was used to carry out the measurements - for both preforms and IPCs, the uni-axial powder press direction in each sample was taken as direction 1, while the two directions orthogonal to this direction were taken as directions 2 and 3, respectively. The three longitudinal (C_{ii}, i = 1–3) and the three shear (C_{ii}, i = 4–6) elastic constants were determined. Group velocities (V_g) of waves were determined by measuring the slopes of the respective phase shift vs. frequency spectra. For the three longitudinal elastic constants C_{11}, C_{22} and C_{33} the longitudinal wave velocities were determined along the directions 1, 2 and 3, respectively. Each shear elastic constant was determined from the average of two different shear wave velocities. For C_{44}, C_{55}, and C_{66} these velocities were V_{23} and V_{32}, V_{13} and V_{31}, and V_{12} and V_{21} (the first suffix denoting the direction of wave propagation and the second suffix denoting the direction of vibration of the particles of the medium [40]), respectively.

2.5. *Measurement of thermal expansion coefficient (CTE)*

Measurement of the thermal expansion behaviour was carried out in a dilatometer DIL 805A/D from Bähr-Thermoanalyse GmbH, Hüllhorst, Germany by measuring the sample length change with temperature. A brief description of the experimental procedure is provided here and for a thorough description we refer to [41]. The studied samples were cylindrical in shape with nominal length of 6 mm and nominal diameter of 4 mm. Thermal expansion was measured by measuring the length change along the long axis of each sample. The specimen was held between two push rods made of alumina. One of the push rods was fixed, the other was connected to a linear variable differential transformer (LVDT) and transmitted the dilatation of the specimen. The specimen was placed in the centre of an induction coil, allowing high heating rates. A thermocouple was spot welded to the sample to measure and record its instantaneous temperature. Four thermal cycles were carried out for each sample between room temperature and 500 °C. Thermal strain measurements were carried out during both heating and cooling at a constant rate of 5 °C/min in an inert helium atmosphere. Before measurement, the two opposite faces of each sample along the direction of strain measurement were polished to ensure plane parallelism when in contact with the measurement rods inside the dilatometer.

To determine the CTE evolution during both heating and cooling, the plot of length change vs. temperature was divided into discrete intervals of 30 °C each. A best fit straight line was fitted to the plot in each interval. Subsequently, the CTE at the mean temperature of each interval was determined following the relation

$$\alpha = \frac{1}{l_0}\left(\frac{dl}{dT}\right)$$

where l_0 is the sample length at the start of each interval and (dl/dT) is the slope of length change vs. temperature plot.

3. Results and discussion

The evolution of both total and open porosity in the porous alumina preforms after sintering as a function of the initial total wax:alumina powder mixture ratio is shown in Fig. 2. Several ceramic preforms for each mixture ratio were produced and the error bars denote one

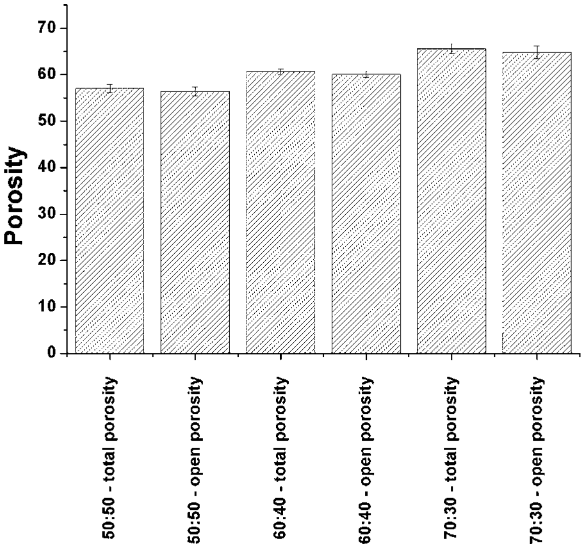

Fig. 2. Variation in total and open porosity in the porous alumina preforms as a function of total wax:alumina powder mixture ratio.

standard deviation among the porosities measured for each mixture ratio. In all cases the error bars are very small, denoting good reproducibility of the data. For any mixture type the difference between the two porosities denotes the amount of closed porosity and in the studied samples this lies in the range of 1 vol%. These closed porosities will not be filled up during melt infiltration and hence they remain as residual porosity in the final composite. As expected, the amount of porosity increases with increasing wax content in the initial powder mixture.

SEM image of the porous preform fabricated using 50:50 mixture ratio of total wax:alumina powders is shown in Fig. 3. The microstructural features of the preforms fabricated using 60:40 and 70:30 mixtures are similar, albeit with a higher porosity. As already discussed in detail in [32], preforms fabricated using a mixture of the VW and CD waxes display a tri-modal pore structure – (a) oval to round shaped large pores resulting from VW, (b) very fine pore network resulting from individual CD particles, and (c) few very large pores (in mm range) resulting from agglomerates of CD formed during initial mixing of the powders.

Fig. 4 shows typical orthogonal slices of the porous preforms fabricated using the three different wax:alumina powder mixture ratios. While the SEM study allows a high resolution 2D structural analysis of the preforms, X-ray computed tomography allows non-destructive 3D imaging of the internal pore structure. The arrow in this figure shows the direction of uni-axial powder pressing. In these grey scale images the pores are denoted in black while the alumina regions are grey. The increase in porosity with increasing wax:alumina ratio, as denoted graphically in Fig. 2, is clearly observed in Fig. 4. The spherical pores resulting from the large VW particles as well as the fine network CD pores are distributed evenly throughout the preform. Additionally, some very large pores resulting from the agglomeration of the CD wax particles are also observed. In all three preforms it is observed that several large pores are flattened along the uni-axial press direction. Thorough discussion of the structural features of such porous bodies studied using X-ray computed tomography was carried out in our earlier work on SiC preforms [31,32] and they will not be repeated here. The elastic properties of the porous preforms processed in this work as well as the composites fabricated therefrom will be discussed in subsequent sections of this paper.

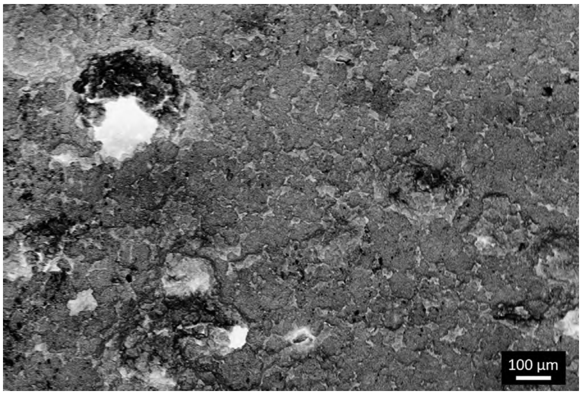

Fig. 3. SEM image of the porous alumina preform fabricated using a total wax: alumina powder mixture of 50:50.

The dependence of density and the three longitudinal elastic constants C_{11}, C_{22} and C_{33} on the initial wax:alumina ratio in the powder mixtures is shown in Fig. 5. For each elastic constant of the three studied samples, measurement of longitudinal sound velocity was repeated thrice. The data points correspond to the average of the elastic constants determined from these three measurements while the standard deviations are denoted as error bars. For all measured elastic constants the error bars are extremely small, denoting excellent reproducibility of the measurements. Both density and the elastic constants decrease with increasing wax:alumina ratio. While density depends solely upon the amount of total porosity in the preforms, the elastic constants depend both on the total porosity and the shape and orientation of the pores with respect to the direction of wave propagation during ultrasonic velocity measurement. For the preform made from 70:30 mixture ratio of wax:alumina, no ultrasonic velocity measurement along preform press direction (i.e. direction 1) was possible as the preform was too fragile and hence for this preform only the two elastic constants C_{22} and C_{33} are provided. Fig. 5 shows that the porous preforms behave as transverse isotropic materials, with the elastic constants C_{22} and C_{33} being almost equal and significantly higher than the elastic constant C_{11}. The observed significantly lower stiffness of the preforms along the preform press direction (i.e. direction 1) follows the trend also observed for SiC preforms reported in [31,32]. Andersson [42] and Huber and Gibson [43] have shown that in porous materials with ellipsoidal pores, the elastic constants are dependent on the aspect ratio of the pores – with the stiffness along the long axis of the pores being significantly higher than the elastic constants transverse to this direction. As the large pores in the studied porous preforms are flattened along direction 1 (i.e. the long axis of the pores are parallel to the direction 1), the elastic constant C_{11} of the preforms is significantly lower than the elastic constants C_{22} and C_{33} (long axis of the pores are in the 2–3 plane of the preforms) and the preforms behave as transverse isotropic materials.

Optical micrographs of the IPCs fabricated by inert gas pressure infiltration of the porous alumina preforms by Al12Si melt are shown in Fig. 6. In these micrographs the ceramic phase is dark while the metallic phase is brighter. As the solubility of aluminium in silicon is negligible at all temperatures [44], the microstructure of the metallic phase in the composite consists of aluminium rich alpha solid solution and essentially pure silicon particles. The silicon particles are distributed primarily in the shape of needles or elongated platelets. The micrographs show that the large pores resulting from spherical VW wax particles as well as the CD agglomerates are completely filled by the metallic alloy. Even the vast majority of the fine network pores of CD are infiltrated. Some residual porosity however remains due to incomplete infiltration of the fine CD pore regions. Measurement of the density of the IPC samples by Archimedes principle allowed the estimation of residual porosity in the composite samples and the maximum residual porosity in the studied IPC samples lied in the range of 3 vol%. This amount of residual porosity is typical for metal/ceramic composites fabricated via casting route [45,46] and may be attributed to the differential thermal contraction of the metallic alloy and the ceramic

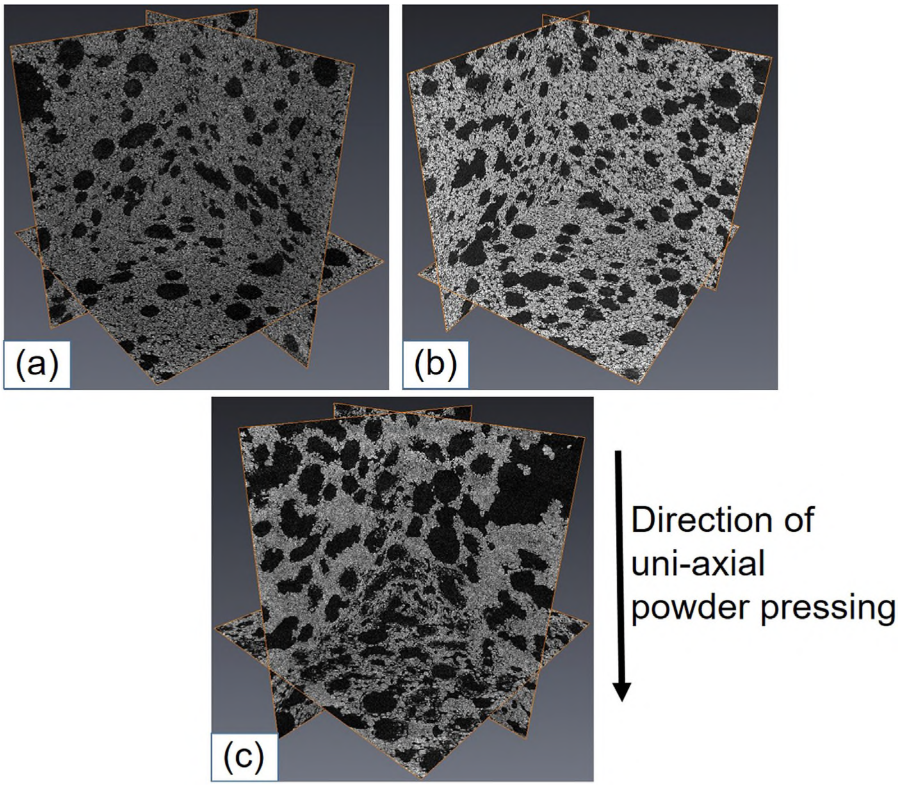

Fig. 4. Representative orthogonal slices obtained from X-ray computed tomography analysis of the porous alumina preforms – (a) wax:alumina = 50:50, (b) wax:alumina = 60:40 and (c) wax:alumina = 70:30. Direction of uni-axial pressing of the powder mixture is shown by the down arrow.

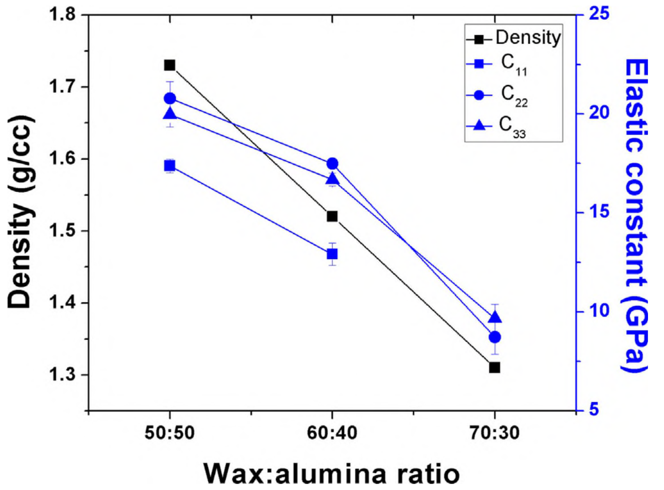

Fig. 5. Evolution of density and longitudinal elastic constants with wax:alumina ratio in the porous preforms.

from the infiltration temperature to room temperature. Typical SEM image of the studied IPC material is shown in Fig. 7. The features of the composite microstructure discussed on the basis of the optical micrographs are visible more clearly in this SEM micrograph. The regions of the metallic alloy, the ceramic phase as well as the fine micropores within the ceramic rich regions are marked.

The three longitudinal and the three shear elastic constants of 17 different composite samples having densities in the range of 2.91 g/cc and 3.18 g/cc were measured. Assuming no porosities in the composite samples and using the bulk densities of Al12Si and alumina to be 2.66 g/cc [28] and 3.90 g/cc [47], respectively; the ceramic contents of the studied samples lied in the range of 20–45 vol%.

Fig. 8 shows the dependence of the longitudinal and shear elastic constants of the composite as a function of sample density. The plots clearly show that apart from some minor deviations, both the longitudinal and shear elastic constants generally increase with increasing density. This behaviour is along the expected lines as both a decrease in residual porosity and an increase in ceramic content in the composite material will increase both the density and the elastic constants. These plots however show that, in individual samples there is no definite trend among the three longitudinal and the three shear elastic constants. It has already been discussed with reference to Fig. 5 that the uninfiltrated alumina preforms show significant anisotropy with the elastic constants along the preform press direction being lower than the directions orthogonal to this direction. The plots in Fig. 8 show that the elastic anisotropy prevalent in the preforms is no more observed in the IPC. Infiltration of the porous alumina preforms by Al12Si improves its stiffness along all directions, with the stiffness enhancement being the highest along the most compliant direction of the preform. This observation of the absence of any pronounced elastic anisotropy in the composite contradicts however our earlier finding on another Al12Si/alumina IPC also fabricated by melt infiltration in porous alumina preforms [28]. The preforms in this earlier study were fabricated using cellulose fibers as pore formers and after uni-axial pressing and sintering the elastic constants of the preforms along uni-axial press direction were significantly lower. Analysis of the elastic properties of the resulting composites however showed that this preform elastic anisotropy was maintained even in the composite although the extent of anisotropy was much weaker. One probable explanation of the lack of any elastic anisotropy in the composite samples studied in this work is the lesser uni-axial pressure applied to the powder mixture during preform fabrication – while 100 MPa pressure was applied for the composites fabricated in [28], only 40 MPa was applied for the composites being studied in this work. The effect of the applied uni-axial pressure on the elastic anisotropy of the porous ceramic preforms was studied in [31] and there it was observed that with increasing uni-axial pressure on the powder mixture the elastic anisotropy of the preforms

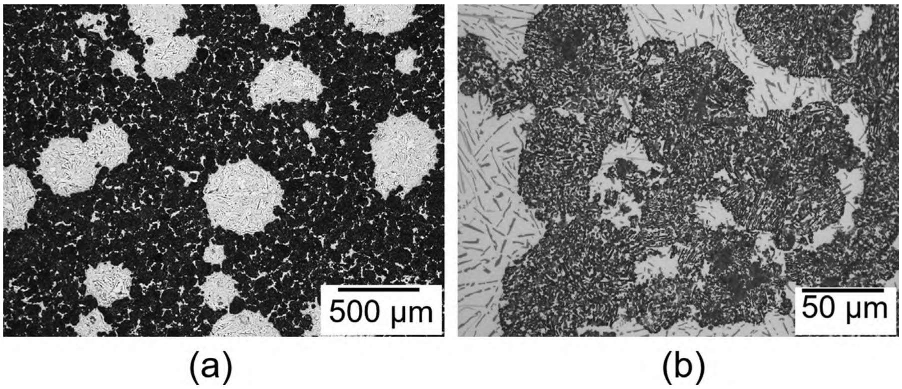

Fig. 6. Optical micrographs of the interpenetrating composites fabricated by gas pressure infiltration of the open porous alumina preforms by Al12Si melt – (a) composite microstructure at a magnification of 50× and (b) composite microstructure at a magnification of 1000×.

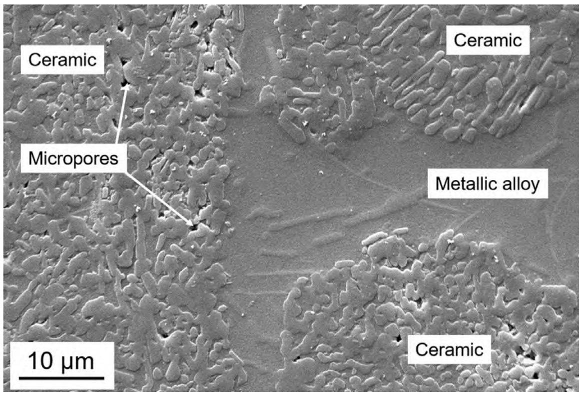

Fig. 7. Typical SEM image of the composite material.

continuously increased.

As no definite trend is observed between the elastic constants of the IPC studied in this work and as in individual samples the three longitudinal and the three shear elastic constants lie very close to each other; hence, for all practical purposes the IPC of the current study may be considered as a quasi-isotropic material with similar values of the elastic constants along all directions. For an isotropic material only two independent elastic constants are necessary to completely define the stiffness tensor of the material [48]. Hence, the average of three longitudinal elastic constants C_{11}, C_{22} and C_{33} as well as the average of the three shear elastic constants C_{44}, C_{55} and C_{66} were used in this work to further determine the more well-known elastic constants of Young's modulus and Poisson's ratio. Standard elasticity relations for isotropic materials, compiled by Berthelot [39], were used for this purpose.

In Fig. 9 the Young's modulus of the IPC determined this way is plotted against sample density. As the average of the three longitudinal elastic constants (C_{11}, C_{22} and C_{33} in Fig. 8 left hand side plot) as well as the three shear elastic constants (C_{44}, C_{55} and C_{66} in Fig. 8 right hand side plot) was used to calculate the composite Young's modulus values plotted in Fig. 9, the calculated values are subject to some standard deviation. The standard deviations between the three longitudinal and the three shear elastic constants were separately calculated. The combined standard deviation for each sample was then determined therefrom and this has been plotted as error bar for each data point in Fig. 9.

Fig. 9 shows that, as with the prior discussion for the longitudinal and shear elastic constants determined directly from UPS, Young's modulus also increases with increasing sample density. Numerous micromechanical models exist for predicting the elastic constants of the composites based on the distribution, amount and properties of the constituent phases of the composite. Correlation between the experimentally determined Young's modulus with the predictions from several micromechanical models are also provided in Fig. 9. Thorough description of the used micromechanical models is beyond the scope of this work and they can be found in the following references [49–53]. The accuracy of the model predictions strongly depend upon the

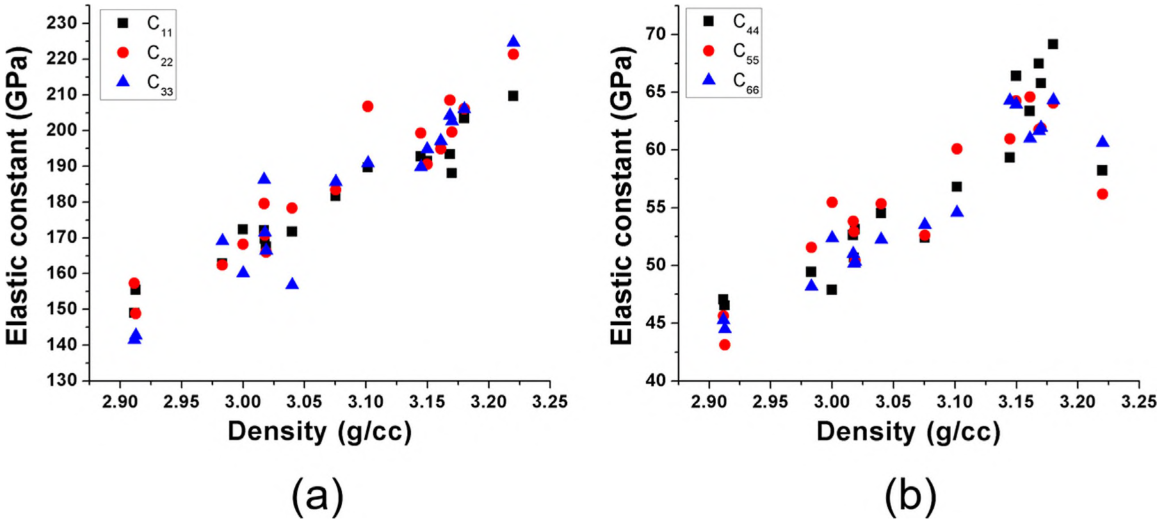

Fig. 8. Dependence of the longitudinal and shear elastic constants of the composites on sample density – (a) plot for longitudinal elastic constants and (b) plot for shear elastic constants.

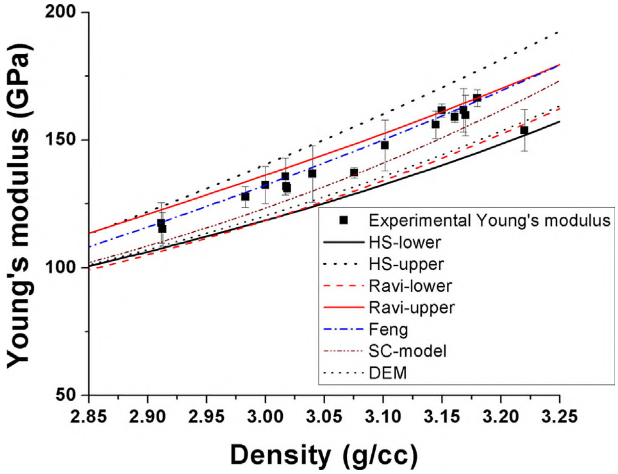

Fig. 9. Correlation between Young's modulus determined in this work experimentally with several theoretical models.

modulus values used for the constituent phases and the assumptions made regarding the presence of porosity in the composite. Additionally, the model predictions consider an ideal interface between the ceramic and the metallic phases. Density of the composites for the model calculations was calculated from rule of mixtures, assuming zero porosity. As in the absence of any coating the interface between alumina and Al12Si is inherently strong [24,54], hence the condition of a strong interface is valid. To calculate the model predictions, the Young's modulus and the Poisson's ratio of alumina were taken as 390 GPa and 0.24, respectively [55]. In an earlier work we determined the elastic constants of an Al12Si alloy similar to the one used in this work using the same UPS method. The corresponding values for Young's modulus and Poisson's ratio were 82 GPa and 0.326, respectively and these values were used in this work for the theoretical calculations. The figure shows that for all the studied samples, the experimentally determined Young's modulus lie between the Hashin–Shtrikman upper and lower bounds. Over the complete range of density of the composite materials studied in this work, the plot shows that the Young's modulus of the composite is best predicted by the Feng model developed in Ref. [51] specifically for interpenetrating phase composites. Moreover, as two independent elastic constants were determined for the isotropic composite materials, even Poisson's ratio of individual samples could be determined from standard expressions for elastic constants of isotropic materials. Poisson's ratio of the studied composite samples were in the range of 0.26–0.32.

Fig. 10 shows the evolution of thermal strain with temperature during all four cycles in an unreinforced Al12Si sample and in three IPC samples with ceramic volume fraction of 0.30, 0.34 and 0.40, respectively. The thermal strain behaviour of Al12Si is reproduced here from an earlier publication [56]. The ceramic volume fractions were calculated assuming zero porosity in the composite samples. Among the samples studied, the residual thermal strain is highest in the unreinforced Al12Si sample – whereby the highest residual strain is observed in the first cycle while for the subsequent cycles, the residual

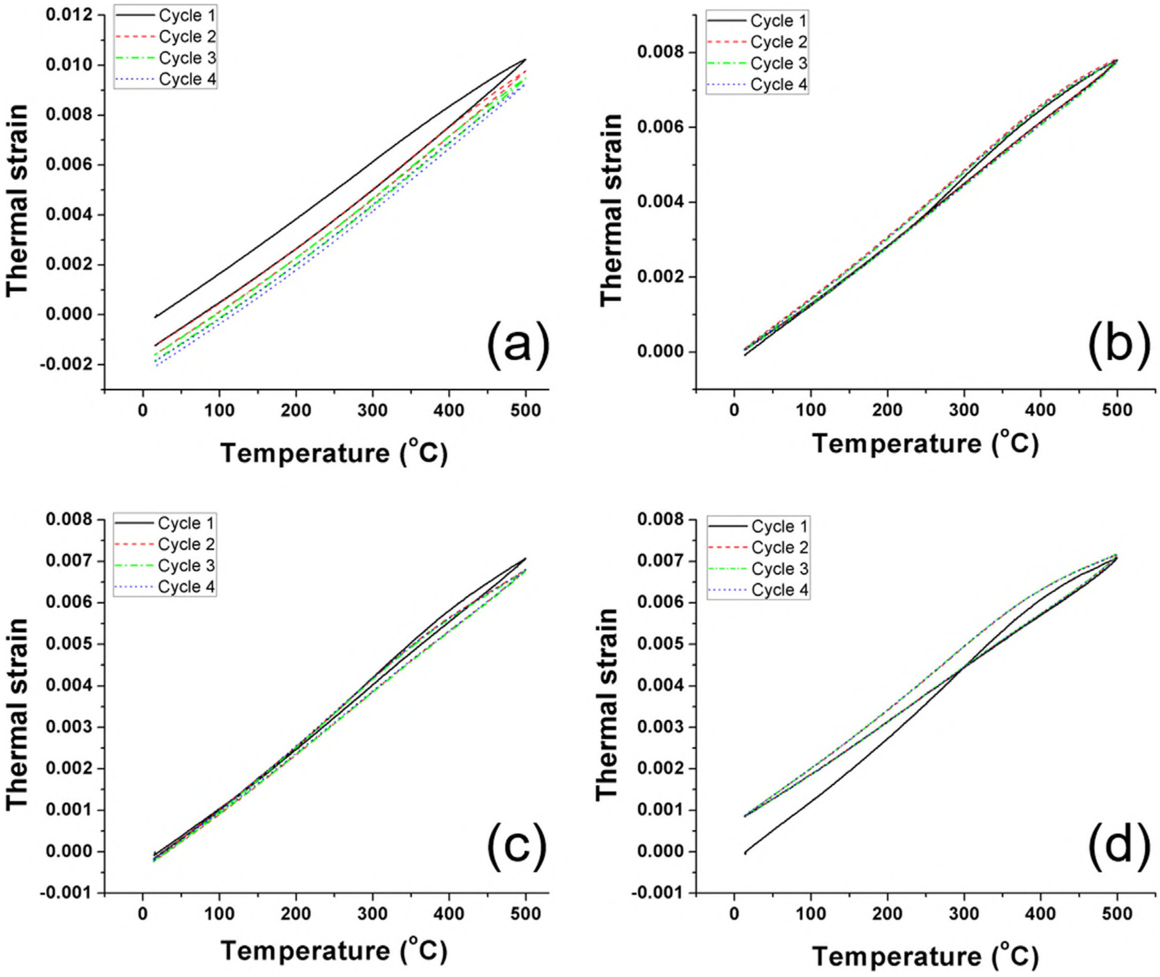

Fig. 10. Evolution of thermal strain with temperature during four thermal cycles in a) unreinforced Al12Si alloy b) IPC with $V_f = 0.30$c) IPC with $V_f = 0.34$ and d) IPC with $V_f = 0.40$.

strain is very less. Apart from the sample with 40 vol% alumina, the other IPC samples show negligibly small thermal residual strain. In the sample with 40 vol% alumina also, the highest residual strain is observed after the first cycle. In all IPC samples, the evolution of thermal strain during cycles 2–4 has a closed form shape. This suggests that during cycles 2–4 the studied IPC samples did not undergo any permanent shape change. This is important for high temperature application of the composite material as dimensional stability after thermal cycling is ensured. The first heating cycle is typically influenced by the processing history and the previous stress state within the material. After slow heating and cooling during the first cycle the material attains a stabilised state and hence the subsequent cycles are more representative of the material behaviour [56,57]. Hence, for all samples the second heating-cooling cycle has been used for further discussion of thermal strain and CTE calculation. As already discussed, the thermal strain curves for the IPC samples in Fig. 10 are characterized by the presence of hysteresis with no residual strain. According to Wu et al. [58], this shape of the thermal strain vs. temperature plot suggests that the thermal stress developed in the material during heating and cooling is just sufficient to yield the material. If the thermal stress is lower than the yield stress, the deformation is completely elastic and correspondingly there should be no thermal hysteresis during thermal cycling. The source of the thermal stress is the incompatibility in CTE between the constituent metallic and the ceramic phases [46,59]. During cooling of the composite material from the processing temperature, due to the higher CTE of the metallic alloy, it will have tensile residual stresses in the as processed state. During heating stage of the thermal cycling, again due to the CTE mismatch between the two phases, compressive stresses start to develop in the metallic matrix. With continued heating, at some point the initial tensile residual stress will be completely cancelled and with further heating, the effective compressive stress in the metallic matrix will continuously increase. At the same time, with increased temperature, the yield strength of the metallic phase continuously decreases. A combination of these two effects will lead to plastic yielding of the metallic alloy phase during thermal cycling at some point, thereby producing the thermal hysteresis in the thermal strain vs. temperature plots.

The evolution of thermal strain with temperature during the second heating cycle in unreinforced Al12Si as well as in the studied IPC samples is shown in Fig. 11. The figure shows that as expected the thermal strain decreases continuously as the ceramic content of the IPC increases.

The evolution of CTE with temperature for unreinforced Al12Si and the three IPC samples during the second heating cycle is shown in Fig. 12. The CTE curve for unreinforced Al12Si initially increases from a room temperature value of approx. 20×10^{-6}/°C to approx. 25×10^{-6}/°C at 330 °C. With a further increase in temperature the CTE of Al12Si continuously decreases. The observed CTE decrease in Al12Si at temperatures higher than 300 °C has also been reported in several other publications where this alloy was used as the metallic phase [46,57]. Hahn and Armstrong [60] studied the thermal expansion behaviour of Al-Si alloys and they attributed the observed decrease to re-dissolution of Si in Al during heating at temperatures above 300 °C.

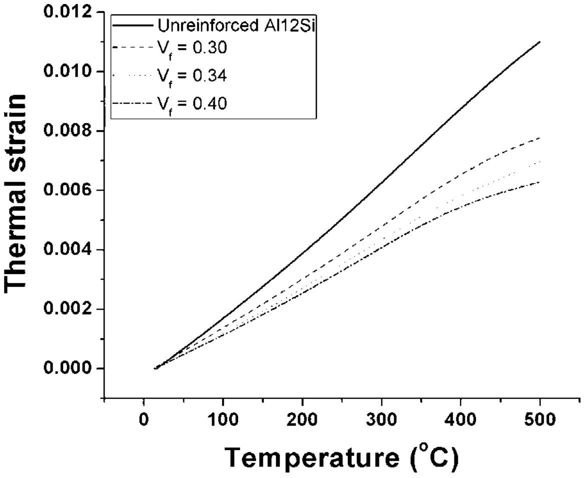

Fig. 11. Evolution of thermal strain with temperature for unreinforced Al12Si and the studied IPC samples during the second heating cycle.

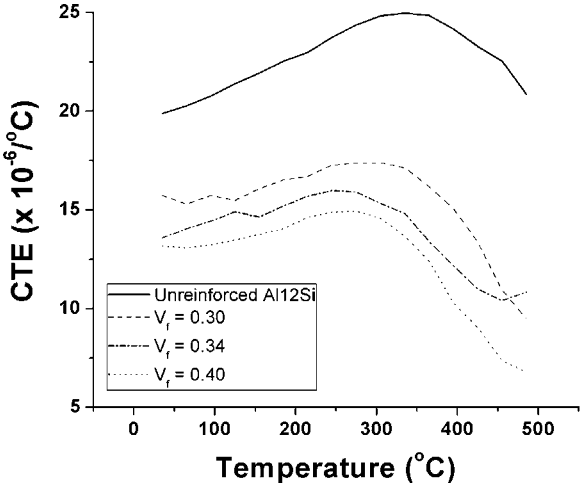

Fig. 12. Evolution of the CTE of unreinforced Al12Si and the studied IPC samples with temperature during the second heating cycle.

Fig. 12 further shows that over the complete temperature range the shapes of the CTE curves of the three IPC samples are similar to the unreinforced metallic alloy. This suggests that the thermal expansion behaviour of the studied composite material is controlled by the metallic alloy. However, as the ceramic content in the composite increases, the CTE curves are shifted to lower CTE values. Huber et al. [46] have studied the influence of the reinforcement phase morphology on the CTE vs. temperature plot of several Al-alloy/SiC composites. Comparing the shapes of the CTE curves obtained in this work with the CTE curves proposed in Ref. [46] it is observed that the thermal expansion behaviour of the studied IPCs resembles more closely the isolated particle reinforced composites. In composites with an interpenetrating structure, as soon as the plastic deformation of the metallic alloy initiates, it starts flowing into the voids present into the three dimensional network structure, and correspondingly the CTE curves show a drop, deviating from the shape of the curve for the unreinforced metallic alloy. The similarity of the CTE evolution observed in this work to isolated particle reinforced composites can probably be attributed to the inhomogeneous microstructure of the studied composite material. As shown in Figs. 4 and 6, the composite microstructure possesses numerous large metallic alloy rich regions at the locations where originally macroscopic pores were present in the ceramic preform from large spherical VW wax or agglomeration of fine CD wax particles. Correspondingly, the microstructure of the studied IPC may be thought of as a combination of soft metallic alloy regions dispersed within ceramic rich regions. As the metallic alloy rich regions are rather large and they being free from the restraining effect of the ceramic reinforcement, it is postulated that these metallic alloy rich regions will expand more during heating and control the thermal expansion behaviour of the overall composite material. The interpenetrating composites studied in [46,61] had a much more uniform distribution of the metallic and the ceramic phases and correspondingly the CTE evolution curves were more representative of a true interpenetrating composite.

Prediction of the thermal expansion behaviour of metal/ceramic composites is complicated as numerous factors such as processing induced residual stresses in both phases, internal stresses developed in the composite during thermal expansion measurement, plastic deformation

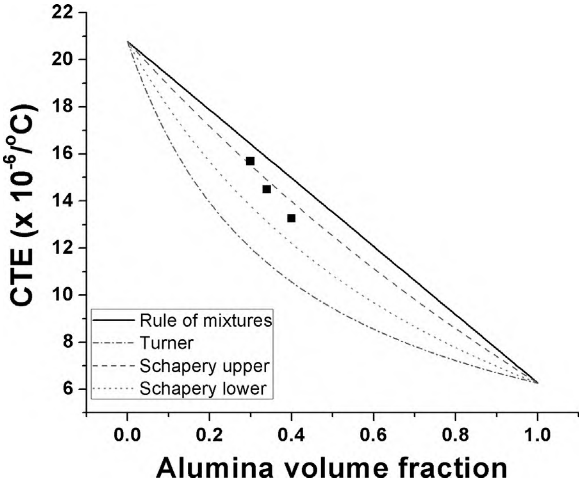

Fig. 13. Comparison of experimentally determined CTE of the composites at 100 °C with theoretical model predictions.

of the metallic phase, development of any damage etc. need to be considered. Numerous theoretical models for the prediction of composite CTE exist. In this work, three such theoretical models – the rule of mixtures model, Turner model and Schapery bounds have been used to predict the CTE of the studied composite material. Thorough theoretical description of these models are beyond the scope of this work and these can be found in relevant literatures [62–64]. Among the used models, the rule of mixtures model is relatively simple as it merely considers the CTEs and volume fractions of the constituent phases. While the upper bound of Schapery represents composites with isolated reinforcements, the Schapery lower bound as well as the Turner model corresponds the CTE of composites with a percolating reinforcement architecture typical for IPCs [46].

Strictly considering, these models are only valid when both the constituent phases of the composite behave linear-elastic. Hence, the experimentally determined CTE of the studied samples at 100 °C, where the samples are deemed to undergo only elastic deformation, has been used for comparison. The calculation of the theoretical model curves requires the elastic constants (Young's modulus, bulk modulus, shear modulus, Poisson's ratio) as well as the CTE of the constituent phases at 100 °C. While the CTE of Al12Si at 100 °C was determined from the experimental curve shown in Fig. 12, CTE of alumina was determined from literature values provided in [65,66]. Elastic constants of Al12Si at 100 °C was unknown and hence the elastic constants of Al7SiMg compiled in [67] have been used for model calculations. The elastic constants of alumina at 100 °C were calculated using the relations summarised by Auerkari [68].

In Fig. 13 the experimentally determined CTE of the studied composite samples during the second heating path is compared with the theoretical models. In this plot the data points denote the experimentally measured CTE of the IPC samples. Fig. 13 shows that the experimentally determined CTE of the studied IPC samples lie between Schapery upper and lower bounds, with the Schapery upper bound being the most accurate. The experimentally measured CTE values are significantly higher than the predictions from Turner model. This further corroborates the fact that the thermal expansion behaviour of the studied IPC samples is more akin to composites reinforced with isolated reinforcement particles than to composites with interpenetrating phase morphology.

The thermal expansion behaviour of the studied composite material shows that apart from only the amount of the individual phases, also the phase morphologies need to be properly tailored to fully exploit the benefits of the percolating ceramic network. In [32] we proposed a simple technique for fabricating open porous ceramic preforms having a wide range of pore morphologies. Infiltration of these preforms will yield metal/ceramic composites consisting of very fine to rather coarse phase distributions. Systematic study of the thermal expansion behaviour of such composites as well as the study of the internal load transfer mechanism in the current composite material will be carried out in future.

4. Summary and conclusions

Thorough analysis of elastic properties as well as the thermal expansion behaviour of a new kind of interpenetrating metal/ceramic composite fabricated by inert gas pressure infiltration of Al12Si melt in porous alumina preforms was carried out. The porous alumina preforms were also fabricated in this work using 1:1 mixture of two different polymer waxes as pore formers. The mixture of ceramic powder and polymer waxes was first pressed uni-axially and then sintered. The resulting preforms displayed a tri-modal pore morphology with pore sizes varying from few microns to even larger than 1 mm. Longitudinal elastic constants of the porous preforms as well as the longitudinal and the shear elastic constants of the composite materials were determined using non-destructive ultrasound phase spectroscopy. The elastic properties of the porous preforms displayed transverse isotropic symmetry with the stiffness being the lowest along the preform press direction. In interpenetrating composites fabricated by melt infiltration no such elastic anisotropy was observed and the composites behaved as quasi-isotropic material. Young's modulus of the composite samples with varying ceramic content were calculated from the measured elastic constants. Comparison with theoretical micromechanical models showed that the Feng model predicted the composite Young's modulus most accurately. Thermal expansion behaviour of the composite material was studied by thermal cycling between room temperature and 500 °C. Both the thermal strain and thermal expansion coefficient decreased with increasing ceramic content. The shapes of the expansion coefficient vs. temperature curves for the composites resembled the unreinforced metallic alloy. In spite of its percolating interpenetrating microstructure, the thermal expansion behaviour of the studied composite samples resembled more closely the composites reinforced with isolated reinforcement particles. The measured thermal expansion coefficients were also higher than the values expected for interpenetrating composites based on theoretical models. These were attributed to the presence of large metallic alloy rich areas in those regions where originally macroscopic pores were present in the ceramic preform from large spherical VW wax or agglomeration of fine CD wax particles.

Acknowledgements

Financial support from the German Research Foundation (DFG) within the Project RO4164/1-1 is gratefully acknowledged. The authors further thank TER HELL & CO. GmbH for supplying the polymer waxes used as pore formers.

Data availability statement

Raw research data used for this publication will be made available on request.

References

[1] N. Chawla, K.K. Chawla, Metal Matrix Composites, Springer, 2013.

[2] T.W. Clyne, P.J. Withers, An Introduction to Metal Matrix Composites, Cambridge University Press, 1995.

[3] A. Mortensen, J. Llorca, Metal matrix composites, Annu. Rev. Mater. Res. 40 (2010) 243–270, https://doi.org/10.1146/annurev-matsci-070909-104511.

[4] W.D. Callister, D.G. Rethwisch, Materials Science and Engineering: An Introduction, John Wiley & Sons Inc, 2010.

[5] A. Abedini, Z.T. Chen, A micromechanical model of particle-reinforced metal matrix composites considering particle size and damage, Comput. Mater. Sci. 85 (2014) 200–205, https://doi.org/10.1016/j.commatsci.2014.01.012.

[6] M. Keneshloo, M. Paidar, M. Taheri, Role of SiC ceramic particles on the physical and mechanical properties of Al-4%Cu metal matrix composite fabricated via mechanical alloying, J. Compos. Mater. 51 (2017) 1285–1298, https://doi.org/10.1177/0021998316673145.

[7] Ö. Savaş, R. Kayikci, Production and wear properties of metal matrix composites reinforced with boride particles, Mater. Des. 51 (2013) 641–647, https://doi.org/10.1016/j.matdes.2013.04.049.

[8] S. Soleymani Shishvan, A.-H. Asghari, Particle size effect in metal matrix composites: a study by the continuum theory of stress gradient plasticity, J. Compos. Mater. 50 (2016) 1717–1723, https://doi.org/10.1177/0021998315595708.

[9] I.T. Lee, Y.Q. Wang, Y. Ochi, S.I. Bae, K.S. Han, J.I. Song, Effect of short fiber reinforcement on the fracture toughness of metal matrix composites, Adv. Compos. Mater. 19 (2010) 41–53, https://doi.org/10.1163/156855109X434801.

[10] G. Garces, G. Bruno, A. Wanner, Load transfer in short fibre reinforced metal matrix composites, Acta Mater. 55 (2007) 5389–5400, https://doi.org/10.1016/j.actamat.2007.06.003.

[11] M. Łągiewka, Mechanical and tribological properties of metal matrix composites reinforced with short carbon fibre, Arch. Metall. Mater. 59 (2014) 707–711, https://doi.org/10.2478/amm-2014-0116.

[12] T. Pacheco, H. Nayeb-Hashemi, H.E.M. Sallam, The effects of matrix and fiber properties on the mechanical behavior and acoustic emission in continuous fiber reinforced metal matrix composites, Mater. Sci. Eng. A 247 (1998) 88–96.

[13] H. Ismar, F. Schröter, F. Streicher, Effects of interfacial debonding on the transverse loading behaviour of continuous fibre-reinforced metal matrix composites, Comput. Struct. 79 (2001) 1713–1722, https://doi.org/10.1016/S0045-7949(01)00097-9.

[14] M. Jacquesson, A. Girard, M.H. Vidal-Sétif, R. Valle, Tensile and fatigue behavior of Al-based metal matrix composites reinforced with continuous carbon or alumina fibers: part I. Quasi-unidirectional composites, Metall. Mater. Trans. A Phys. Metall. Mater. Sci. 35 (2004) 3289–3305, https://doi.org/10.1007/s11661-004-0071-2.

[15] M. Kouzeli, D.C. Dunand, Effect of reinforcement connectivity on the elasto-plastic behavior of aluminum composites containing sub-micron alumina particles, Acta Mater. 51 (2003) 6105–6121, https://doi.org/10.1016/S1359-6454(03)00431-2.

[16] H. Prielipp, M. Knechtel, N. Claussen, S.K. Streiffer, H. Müllejans, M. Rühle, J. Rödel, Strength and fracture toughness of aluminum/alumina composites with interpenetrating networks, Mater. Sci. Eng. A 197 (1995) 19–30, https://doi.org/10.1016/0921-5093(94)09771-2.

[17] M. Sternitzke, M. Knechtel, M. Hoffmann, E. Broszeit, J. Roedel, Wear properties of alumina/aluminum composites with interpenetrating networks, J. Am. Ceram. Soc. (1996) 121–128.

[18] G. Roudini, R. Tavangar, L. Weber, A. Mortensen, Influence of reinforcement contiguity on the thermal expansion of alumina particle reinforced aluminium composites, Int. J. Mater. Res. (2010) 1113–1120.

[19] H.J. Feng, J.J. Moore, In situ combustion synthesis of dense ceramic and ceramic-metal interpenetrating phase composites, Metall. Mater. Trans. B 26 (1995).

[20] W. Liu, U. Köster, Microstructures and properties of interpenetrating alumina/aluminium composites made by reaction of SiO_2 glass preforms with molten aluminium, Mater. Sci. Eng. A 210 (1996) 1–7, https://doi.org/10.1016/0921-5093(95)10078-4.

[21] D. Horvitz, I. Gotman, E.Y. Gutmanas, N. Claussen, In situ processing of dense Al_2O_3-Ti aluminide interpenetrating phase composites, J. Eur. Ceram. Soc. 22 (2002) 947–954, https://doi.org/10.1016/S0955-2219(01)00396-X.

[22] X. qing Xie, D. Zhang, T. xiang Fan, T. Sakata, H. Mori, T. Okabe, T. Hirose, The fabrication of composites with interpenetrating networks based on woodceramics, Mater. Lett. 56 (2002) 102–107, https://doi.org/10.1016/S0167-577X(02)00426-3.

[23] C. San Marchi, M. Kouzeli, R. Rao, J.A. Lewis, D.C. Dunand, Alumina-aluminum interpenetrating-phase composites with three-dimensional periodic architecture, Scr. Mater. 49 (2003) 861–866, https://doi.org/10.1016/S1359-6462(03)00441-X.

[24] S. Roy, B. Butz, A. Wanner, Damage evolution and domain-level anisotropy in metal/ceramic composites exhibiting lamellar microstructures, Acta Mater. 58 (2010), https://doi.org/10.1016/j.actamat.2009.12.015.

[25] S. Roy, A. Wanner, Metal/ceramic composites from freeze-cast ceramic preforms: domain structure and elastic properties, Compos. Sci. Technol. 68 (2008), https://doi.org/10.1016/j.compscitech.2007.06.013.

[26] S. Roy, J. Gibmeier, A. Wanner, In situ study of internal load transfer in a novel metal/ceramic composite exhibiting lamellar microstructure using energy dispersive synchrotron X-ray diffraction, Adv. Eng. Mater. 11 (2009), https://doi.org/10.1002/adem.200800352.

[27] S. Roy, J. Gibmeier, V. Kostov, K.A. Weidenmann, A. Nagel, A. Wanner, Internal load transfer in a metal matrix composite with a three-dimensional interpenetrating structure, Acta Mater. 59 (2011), https://doi.org/10.1016/j.actamat.2010.11.004.

[28] S. Roy, O. Stoll, K.A. Weidenmann, A. Nagel, A. Wanner, Analysis of the elastic properties of an interpenetrating AlSi12-Al2O3 composite using ultrasound phase spectroscopy, Compos. Sci. Technol. 71 (2011), https://doi.org/10.1016/j.compscitech.2011.02.014.

[29] S. Roy, J. Gibmeier, V. Kostov, K.A. Weidenmann, A. Nagel, A. Wanner, Internal load transfer and damage evolution in a 3D interpenetrating metal/ceramic composite, Mater. Sci. Eng. A 551 (2012), https://doi.org/10.1016/j.msea.2012.05.016.

[30] K. Sang, Y. Weng, Z. Huang, X. Hui, H. Li, Preparation of interpenetrating alumina-copper composites, Ceram. Int. 42 (2016) 6129–6135, https://doi.org/10.1016/j.ceramint.2015.12.174.

[31] S. Roy, K.G. Schell, E.C. Bucharsky, K.A. Weidenmann, A. Wanner, M.J. Hoffmann, Characterization of elastic properties in porous silicon carbide preforms fabricated using polymer waxes as pore formers, J. Am. Ceram. Soc. 96 (2013), https://doi.org/10.1111/jace.12341.

[32] S. Roy, K.G. Schell, E.C. Bucharsky, P. Hettich, S. Dietrich, K.A. Weidenmann, A. Wanner, M.J. Hoffmann, Processing and elastic property characterization of porous sic preform for interpenetrating metal/ceramic composites, J. Am. Ceram. Soc. 95 (2012), https://doi.org/10.1111/j.1551-2916.2012.05347.x.

[33] S. Roy, J.-M. Gebert, G. Stasiuk, R. Piat, K.A. Weidenmann, A. Wanner, Complete determination of elastic moduli of interpenetrating metal/ceramic composites using ultrasonic techniques and micromechanical modelling, Mater. Sci. Eng. A 528 (2011), https://doi.org/10.1016/j.msea.2011.07.029.

[34] S. Roy, A. Wanner, T. Beck, T. Studnitzky, G. Stephani, Mechanical properties of cellular solids produced from hollow stainless steel spheres, J. Mater. Sci. 46 (2011), https://doi.org/10.1007/s10853-011-5496-6.

[35] A. Wanner, Elastic modulus measurements of extremely porous ceramic materials by ultrasonic phase spectroscopy, Mater. Sci. Eng. A 248 (1998) 35–43, https://doi.org/10.1016/S0921-5093(98)00524-3.

[36] C. Ting, W. Sachse, Measurement of ultrasonic dispersion by phase comparison of continuous harmonic waves, J. Acoust. Soc. Am. 64 (1978) 852–857.

[37] L. Lynnworth, E. Papadakis, W.R. Rea, Ultrasonic measurement of phase and group velocity using continuous wave transmission techniques, 1973.

[38] E. Papadakis, Ultrasonic velocity and attenuation: measurement methods with scientific and industrial applications, Phys. Acoust. XII (1976) 277–374.

[39] J.-M. Berthelot, Composite Materials: Mechanical Behavior and Structural Analysis, Springer-Verlag, Berlin, Heidelberg, 1999.

[40] J.L. Rose, Ultrasonic Waves in Solid Media, Cambridge University Press, 1999.

[41] D. Kaiser, B. de Graaff, S. Dietrich, V. Schulze, A novel procedure to account for high temperature gradients in an induction dilatometer sample during rapid heating, Thermochim. Acta 646 (2016) 8–15, https://doi.org/10.1016/j.tca.2016.10.014.

[42] C. Andersson, Derivation of the exponential relation for the effect of ellipsoidal porosity on elastic modulus, J. Am. Ceram. Soc. 79 (1996) 2181–2184.

[43] A. Huber, L. Gibson, Anisotropy of foams, J. Mater. Sci. 23 (1988) 3031–3040.

[44] J. Davies, ASM Specialty Handbook on Aluminum and Aluminum Alloys, ASM International, 1996.

[45] S. Roy, Metal/Ceramic Composites from Freeze-Cast Preforms: Domain Structure and Mechanical Properties, University of Karlsruhe (TH), 2009.

[46] T. Huber, H.P. Degischer, G. Lefranc, T. Schmitt, Thermal expansion studies on aluminium-matrix composites with different reinforcement architecture of SiC particles, Compos. Sci. Technol. 66 (2006) 2206–2217, https://doi.org/10.1016/j.compscitech.2005.12.012.

[47] J.V. Connolly, Engineered Materials Handbook, Vol 1. Composites 1 ASM International, 1987.

[48] J. Nye, Physical Properties of Crystals, Oxford University Press, 1985.

[49] Z. Hashin, S. Shtrikman, A variational approach to the theory of the elastic behaviour of multiphase materials, J. Mech. Phys. Solids 11 (1963) 127–140.

[50] K. Ravichandran, Elastic properties of two-phase composites, J. Am. Ceram. Soc. 77 (1994) 1178–1184.

[51] X. Feng, Z.H.I. Tian, Y. Liu, S. Yu, Effective elastic and plastic properties of interpenetrating multiphase composites, Appl. Compos. Mater. 11 (2004) 33–55.

[52] S. Torquato, Random Heterogeneous Materials: Microstructure and Macroscopic Properties, Springer, 2002.

[53] R. Hill, A self-consistent mechanics of composite materials, J. Mech. Phys. Solids 13 (1965) 213–222.

[54] M. Hu, J. Yang, H. Cao, A. Evans, R. Mehrabian, The mechanical properties of Al alloys reinforced with continuous Al_2O_3 fibers, Acta Metall. Mater. 40 (1992) 2315–2326.

[55] ASM International. Handbook Committee, Engineered Materials Handbook, Vol 1. Composites, (1987).

[56] S. Roy, P. Albrecht, L. Przybilla, K.A. Weidenmann, M. Heilmaier, A. Wanner, Effect of phase architecture on the thermal expansion behavior of interpenetrating metal/ceramic composites, Ceram. Trans. 240 (2013) 33–43, https://doi.org/10.1002/9781118744109.ch4.

[57] K. Lichtenberg, K.A. Weidenmann, Effect of reinforcement size and orientation on the thermal expansion behavior of metallic glass reinforced metal matrix composites produced by gas pressure infiltration, Thermochim. Acta 654 (2017) 85–92, https://doi.org/10.1016/j.tca.2017.05.010.

[58] S.Q. Wu, Z.S. Wei, S.C. Tjong, The mechanical and thermal expansion behavior of an Al-Si alloy composite reinforced with potassium titanate whisker, Compos. Sci. Technol. 60 (2000) 2873–2880, https://doi.org/10.1016/S0266-3538(00)00160-3.

[59] N. Chen, H. Zhang, M. Gu, Y. Jin, Effect of thermal cycling on the expansion behavior of Al/SiCp composite, J. Mater. Process. Technol. 209 (2009) 1471–1476, https://doi.org/10.1016/j.jmatprotec.2008.03.054.

[60] T.A Hahn, R.W. Armstrong, Internal stress and solid solubility effects on the thermal expansivity of AI-Si eutectic alloys, Int. J. Thermophys. 9 (1988) (1).

[61] S. Skirl, M. Hoffmann, K. Bowman, S. Wiederhornp, J. Roedel, Thermal expansion behavior and macrostrain of Al_2O_3/Al composites with interpenetrating networks, Acta Metall. 46 (1998) 2493–2499.

[62] A. Kelly, C. Zweben, T.W. Clyne, Comprehensive composite materials, Metal Matrix Composites 3 Elsevier Science, Oxford, UK, 2000.

[63] P. Turner, Thermal expansion stresses in reinforced plastics, J. Res. Natl. Bur. Stand. 37 (1946) 240–250 (1934).

[64] R.A. Schapery, Thermal expansion coefficients of composite materials based on energy principles, J. Compos. Mater. 2 (1968) 380–404, https://doi.org/10.1177/002199836800200308.

[65] B. Yates, R.F. Cooper, A.F. Pojur, Thermal expansion at elevated temperatures. II. Aluminium oxide: experimental data between 100 and 800 K and their analysis, J. Phys. C Solid State Phys. 5 (1972) 1046–1058, https://doi.org/10.1088/0022-3719/5/10/009.

[66] D. De Faoite, D.J. Browne, F.R. Chang-Díaz, K.T. Stanton, A review of the processing, composition, and temperature-dependent mechanical and thermal properties of dielectric technical ceramics, J. Mater. Sci. 47 (2012) 4211–4235, https://doi.org/10.1007/s10853-011 − 6140-1.

[67] T. Huber, Thermal Expansion of Aluminum Alloys and Composites, TU Wien, 2003.

[68] P. Auerkari, Mechanical and Physical Properties of Engineering Alumina Ceramics, 1996.